

# Correlated helimagnetic configuration in a nonsymmorphic magnetic nodal semimetal

Xi Luo<sup>1,\*</sup>, Yu-Ge Chen<sup>2,\*</sup>, Ye-Min Zhan<sup>3</sup>, and Yue Yu<sup>3†</sup>

1. College of Science,  
University of Shanghai for Science and Technology,  
Shanghai 200093, China

2. Institute for Quantum Science and Technology,  
Department of Physics, Shanghai University,  
Shanghai 200444, China

3. State Key Laboratory of Surface Physics and Department of Physics,  
Fudan University, Shanghai 200433, China

(Dated: April 1, 2025)

Nonsymmorphic magnetic Weyl semimetal materials such as ReAlX (Re=rare earth, X=Si/Ge) provide a unique opportunity to explore the correlated phenomena between Weyl fermions and nontrivial magnetic configurations. To be specific, we study a lattice model in which the magnetic configuration is determined by the competition among ferromagnetic (FM) interaction, the Dzyaloshinsky-Moriya interaction, and the Kondo coupling  $K_0$  to the Weyl fermion. Both quantum and finite-temperature phase transitions between FM and correlated nesting helical configurations are found. Different from the uncorrelated helimagnet that decouples from the Weyl fermions, this correlated helimagnet induces a magnetic Brillouin zone with a  $K_0$ -dependent nesting in the band structure of the conduction electrons instead of the monopole-like Weyl cone. By measuring the current induced by the chiral magnetic effect on the conduction electron with nesting Weyl nodes, one can distinguish the correlated nesting helical order from the ferromagnetism because the chiral magnetic effect is considerably suppressed in the former case. These properties we find here may explain the experimental observations in ReAlX.

*Introduction.* Recently, the nodal semimetals in a set of nonsymmorphic magnetic materials, ReAlX (Re=rare earth, X=Si/Ge), attract widespread attention [1–4] and a type of Weyl semimetals with breaking both the time-reversal  $\Theta$  and inversion  $P$  symmetries was found in ReAlX [5–14]. These magnetic materials belong to the body-centered tetragonal crystal system with a non-centrosymmetric space group  $I4_1md$ . Due to the  $P$  breaking, the Weyl nodes possess different energies. Meanwhile, the  $f$ -orbital electrons of the rare earth elements provide a strong magnetic moment, so that a strong Ruderman-Kittel-Kasuya-Yosida (RKKY) interaction can exist by mediating Weyl fermions. The RKKY interaction induces competition among the Heisenberg, Kitaev-Ising, and Dzyaloshinsky-Moriya (DM) interactions [15–17], which leads to the emergence of several nontrivial magnetic configurations, such as spiral, helical, hedgehog, skyrmion, and meron-antimeron pairs [18].

The ReAlX materials provide a unique opportunity to study the correlated phenomena that come from the interplay between Weyl fermions and nontrivial magnetic configurations through the Kondo coupling [19], e.g., new exotic phenomena such as the topological Hall effect and room temperature anomalous Hall effect [10, 12]. This raises the possibility of preparing high-density ultra-fast storage devices with these materials [20–24].

Physically, those nontrivial magnetic orders rotate the

Weyl fermion’s spin configuration in real space via the Kondo coupling, which competes with the monopole topology of the Weyl nodes in momentum space. This competition may further induce new correlated phenomena and correlated topological states of matter that lack clear explanations yet.

In this Letter, we focus on the correlated nesting helical magnetic configuration (CNHMC), which has been observed in ReAlX materials. For example, since the ratio between out-of-plane and in-plane magnetic susceptibility  $\chi_c/\chi_a$  is very close in SmAlSi at  $2K$ , a helimagnet with  $\mathbf{Q} = \frac{2\pi}{3}(0.979, 0.979, 0)$  emerges, which is consistent with the nesting vector between Weyl nodes [10]. In CeAlGe, a phase transition from the canted magnetic order to helimagnet was observed at  $4.5K$ . The helimagnet also provides a nesting vector between the Weyl nodes and stabilizes magnetic fluctuations from the magnetic transition temperature to the Curie temperature [9]. This phase transition to the helimagnet and the CNHMC effect are also reported for PrAlSi [5], NdAlSi [6, 7], CeAlSi [8], and NdAlGe [11].

However, the mechanism of the magnetic phase transition and the origin of the emergence of the CNHMC in those materials remain unclear. The specific mechanism behind the anomalous transport phenomena observed near  $T = 12.8K$  in CeAlGe [9], such as the nearly zero magnetoresistance, the switch from negative to positive magnetoresistance, and the maximal suppression of thermal conductivity by magnetic fields is not yet fully understood. In Ref. [9], in which two of the present authors joined, a phenomenological analysis of these properties was partially done by assuming uncorrelated Weyl

\*These two authors contribute equally.

†Correspondence to: yuyue@fudan.edu.cn

node nesting, but studies on the CNHMC and the magnetic phase transition are lacking.

Conventionally, the magnetic configuration  $\mathbf{M}$  and Weyl fermions are separately studied. However, in ReAlX, the strong Kondo coupling plays an important role, so this separated treatment is not valid. In this Letter, we find that the strong coupling problem is exactly solvable at the Fermi surface. We then take this correlated  $\mathbf{M}$  configuration as a background field to deal with the conduction electrons. When we determine the phase diagram of the correlated magnetism, we fix the fermion spin configuration. With these approximations, we see the phase transitions from an ordered phase, e.g., the ferromagnetic (FM) one, to the CNHMC both at zero temperature and finite temperature. We calculate the current induced by the chiral magnetic effect (CME) both in the FM phase and the CNHMC and find that the current for the latter is an order of magnitude less than that for the former. This may explain the nearly zero magnetoresistance near  $T = 12.8\text{K}$  in CeAlGe [9].

*Lattice model.* The common model study for the materials ReAlX starts from the calculation of the band structure of this body-centered tetragonal crystal system with a non-centrosymmetric space group  $I4_1md(109)$ . The Weyl nodes are found near the Fermi level and are coupled to the local moment from the  $f$ -electron in the rare-earth element. Such a strategy is fine but difficult to understand the basic physics due to the complicated numerics.

Due to the crystal symmetry and observed large anomalous Hall effects [5, 8, 11–13], the conduction electrons in ReAlX are Weyl semimetals with both  $\Theta$  and  $P$  symmetry breaking. To see the basic physics behind the numerics, we study a simplified cubic lattice model in which the conduction electrons are Weyl semimetals without  $\Theta$  and  $P$  symmetries and have two Weyl nodes that are adjusted to be near the Fermi level. The electrons couple to  $\mathbf{M}_i$  via the Kondo coupling while the nearest neighbor  $\mathbf{M}_i$  and  $\mathbf{M}_j$  are coupled through the FM Heisenberg and the DM interactions:

$$\begin{aligned} H &= H_W + H_K + H_H + H_{DM}, \\ H_W &= \sum_j [(-t_x c_j^\dagger \sigma_z c_{j+\hat{x}} - t_y c_j^\dagger \sigma_z c_{j+\hat{y}} - t_z c_j^\dagger \sigma_z c_{j+\hat{z}} \\ &\quad - it'_x c_j^\dagger \sigma_x c_{j+\hat{x}} - it'_y c_j^\dagger \sigma_y c_{j+\hat{y}} - iv_0 c_j^\dagger \sigma_0 c_{j+\hat{z}} \\ &\quad + h.c.) + mc_j^\dagger \sigma_z c_j], \\ H_K &= \sum_j K_0 \mathbf{s}_j \cdot \mathbf{M}_j, \quad H_H = \sum_{\langle ij \rangle} J_0 \mathbf{M}_i \cdot \mathbf{M}_j, \\ H_{DM} &= \sum_{\langle ij \rangle} \mathbf{D}_0 \cdot \mathbf{M}_i \times \mathbf{M}_j. \end{aligned} \quad (1)$$

For simplicity, we restrict  $H_W$  to be a minimal two-band model [25, 26] and the Weyl nodes are located at  $(0, 0, \pm k_0)$  with  $\cos k_0 = (m/2 - t_x - t_y)/t_z$ .  $c_j^\dagger$  (the spin index omitted) is the creation operator of the conduction electron at site  $j$  whose spin  $\mathbf{s}_j = \frac{1}{2} c_j^\dagger \boldsymbol{\sigma} c_j$ .

For the FM case,  $J_0 < 0$ . In the following, we use  $t_x = t_y = t_z = t'_x = t'_y = t = 1$ ,  $m = 5t$  and  $k_0 = \pi/3$ . The chemical potential has been set to zero.  $H_K$  is the on-site Kondo coupling between  $\mathbf{s}_i$  and  $\mathbf{M}_i$  with the coupling strength  $K_0$ .  $H_H$  and  $H_{DM}$  are the nearest-neighbor FM Heisenberg and DM interactions, respectively.

When solving the conduction electron problem, we use the adiabatic approximation, i.e., assuming the conduction electrons are fast-moving with respect to the fluctuations of  $\mathbf{M}$  when  $\mathbf{M}$  is considered a background. On the other hand, the configuration of  $\mathbf{M}$  is determined by the competition of the variational ground state energies when the conduction electron spin is assumed to be polarized by  $\mathbf{M}$ 's configuration, the CNHMC or FM.

For the helical magnetic configuration, without loss of generality, one takes  $\mathbf{M} = (\sin[Qz], \cos[Qz], 0)$ . The Hamiltonian for Weyl fermions with the Kondo coupling becomes

$$\begin{aligned} H_0 &= H_W + H_K \\ &= \sum_{\mathbf{k}, \sigma} [(m - 2t_x \cos k_x - 2t_y \cos k_y \\ &\quad - 2t_z \cos k_z) c_\sigma^\dagger(\mathbf{k}) \sigma_z c_\sigma(\mathbf{k}) + 2t'_x \sin k_x c_\sigma^\dagger(\mathbf{k}) \sigma_x c_\sigma(\mathbf{k}) \\ &\quad + 2t'_y \sin k_y c_\sigma^\dagger(\mathbf{k}) \sigma_y c_\sigma(\mathbf{k}) + 2v_0 \sin k_z c_\sigma^\dagger(\mathbf{k}) \sigma_0 c_\sigma(\mathbf{k}) \\ &\quad + (c_\uparrow^\dagger(k_x, k_y, Q + k_z)(-i\frac{K_0}{2})c_\downarrow(k_x, k_y, k_z) + h.c.)], \end{aligned} \quad (2)$$

where  $\uparrow$  and  $\downarrow$  are the spin indices. The last term in Eq. (2) is the Kondo coupling between the Weyl fermion and the helical magnetic configuration. Notice that the momentum shift from  $k_z$  to  $k_z \pm Q$  comes from the helical wave number  $Q$ .

*Continuum limit and CNHMC effects.* Before going to the numerical calculations for the lattice model, we consider the continuum limit of Eq. (2) to show that the correlated helimagnet is an allowed magnetic ground state configuration. When  $|Q| \ll 2|k_0|$ , due to the energy offset  $b_0$  between the two Weyl nodes in a non-centrosymmetric system, we can integrate out one Weyl fermion that is below the chemical potential, say,  $\psi_-$ . The effective equations of motion of  $\mathbf{M}$  and the conduction electron  $\psi = \psi_+$  at a given Weyl valley in the continuum limit are given by [27, 28]

$$\begin{aligned} -i\boldsymbol{\sigma} \cdot (\nabla + i\frac{K_0}{2}\mathbf{M})\psi &= E_e \psi, \\ K_0 \mathbf{s} + \frac{D}{2} \nabla \times \mathbf{M} - J \nabla^2 \mathbf{M} &= 0, \end{aligned} \quad (3)$$

where  $J \propto K_0^2 - 2J_0$  and  $D \propto v_- K_0^2 + 4D_0$  [29, 30]. In the correlated case, the helimagnet remains an exact  $E_e = 0$  solution with  $Q = \frac{D \pm \sqrt{D^2 + 16JK_0}}{4J}$ , which reduces to the uncorrelated helimagnet or the FM when  $K_0 = 0$  i.e., either  $Q = |\mathbf{Q}| = |D/2J|$  and or  $Q = 0$  [31]. When  $K_0 \neq 0$ ,  $\mathbf{M}$  and  $\psi$  are correlated via the Kondo coupling. The energy spectrum of the conduction electron  $\psi$  is shown in Fig. 1. The zero mode solutions are localized

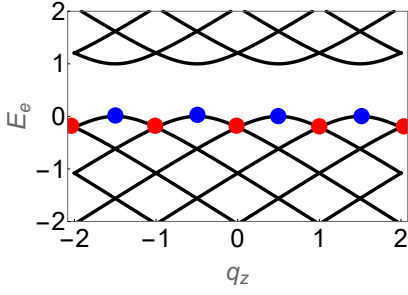


FIG. 1: (color online) The energy spectrum in the continuum limit for Weyl fermions coupled with a helimagnet along the  $q_z$ -direction. We set  $Q = K_0 = 1$ . The helimagnet introduces a magnetic Brillouin zone. The red points stand for the Weyl nodes and the blue points stand for the zero modes (see [28]).

at the boundaries of the magnetic Brillouin zone which is introduced due to the helimagnet (For details, see [28]).

When  $\mathbf{Q}$  of the helimagnet forms a commensurate nesting vector between the Weyl nodes, the helimagnet becomes a CNHMC. This nesting effect has been used to explain the experimental results in CeAlGe [9], but the uncorrelated helimagnet state is not available in ReAlX. By considering the CNHMC, the low-energy effective Hamiltonian of the conduction electron reads  $H'_{eff} = \sum_{\mathbf{k}} \Phi_{\mathbf{k}}^\dagger h'_{\mathbf{k}} \Phi_{\mathbf{k}}$ , where

$$h'_{\mathbf{k}} = k'_x \sigma_x \tau_0 + k'_y \sigma_y \tau_0 + k'_z \sigma_z \tau_z + a_0 k'_z \sigma_0 \tau_0 + b_0 \sigma_0 \tau_z + K_0 \sigma_y \tau_x / 2, \quad (4)$$

and  $\Phi = (c_{+\uparrow}, c_{+\downarrow}, c_{-\uparrow}, c_{-\downarrow})$  with  $\pm$  labeling two Weyl valleys;  $\sigma$  and  $\tau$  are the matrices that act on spin and valley indices, respectively.  $k'_x = 2t'_x k_x$ ,  $k'_y = 2t'_y k_y$ ,  $k'_z = 2t_z (\sin k_0) k_z$ ,  $a_0 = v_0 (\cot k_0) / t$ , and  $b_0 = 2v_0 (\sin k_0)$ . The spectra of Hamiltonian (4) read  $E_{\pm, \pm} = a_0 k'_z$

$\pm \sqrt{\mathbf{k}'^2 + (K_0/2)^2 + b_0^2} \pm \sqrt{K_0^2 (k_y'^2 + k_z'^2) + 4b_0^2 \mathbf{k}'^2}$ . In the  $K_0 \rightarrow 0$  limit,  $b_0$  becomes the energy offset between the two Weyl nodes, and  $a_0$  controls the type of the Weyl node.

*Band structures of the fermion.* We now turn back to the lattice model. Similar to dealing with integer quantum Hall effects with the lattice model [32–34] (also see [35] for a brief review), one defines  $|\Psi\rangle = \sum_{j=1}^q \psi_j c^\dagger(k_x, k_y, k_z^0 + Qj)|0\rangle$ , where  $Q = 2\pi p/q$  with  $p$  and  $q$  coprime,  $k_z = k_z^0 + Qj$ , and  $\psi_{j+q} = \psi_j$ . Then, the Schrödinger equation  $H_0|\Psi\rangle = E|\Psi\rangle$  is reduced to the Harper equations

$$\begin{aligned} & [m - 2t_x \cos k_x - 2t_y \cos k_y - 2t_z \cos(k_z^0 + Qj)] \sigma_z \psi_j \\ & + 2t'_x \sin k_x \sigma_x \psi_j + 2t'_y \sin k_y \sigma_y \psi_j + 2v_0 \sin(k_z^0 + Qj) \psi_j \\ & + (i \frac{K_0}{2}) ((\frac{\sigma_z - 1}{2}) \psi_{j-1} + (\frac{\sigma_z + 1}{2}) \psi_{j+1}) \\ & = E(k_x, k_y, k_z^0) \psi_j. \end{aligned} \quad (5)$$

The Harper equations have  $q$  eigenvalues for a given  $(k_x, k_y, k_z^0)$ . The original band is split into  $q$  subbands due to the Kondo coupling to the CNHMC, and each

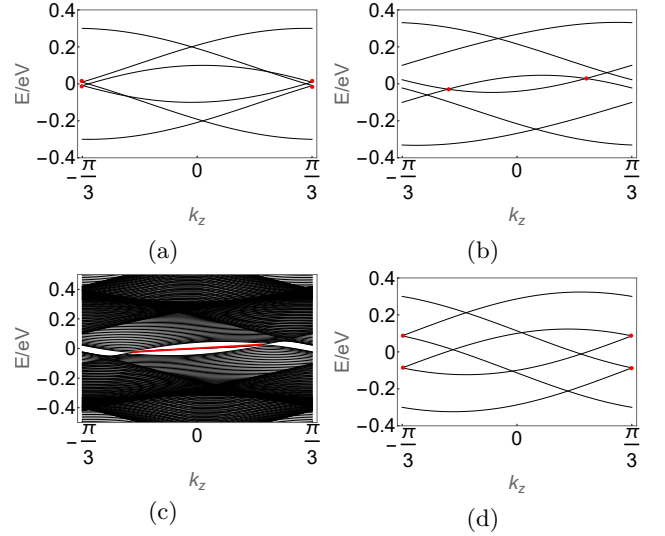


FIG. 2: (color online) The band structures of Weyl fermions with the CNHMC.  $Q = 2\pi/3$ ,  $t = t' = 0.1\text{eV}$ , and  $k_x = k_y = 0$ . (a)  $K_0 = 10\text{meV}$ ,  $v_0 = 5\text{meV}$ . (b)  $K_0 = 200\text{meV}$ ,  $v_0 = 5\text{meV}$ . (c)  $K_0 = 200\text{meV}$ ,  $v_0 = 5\text{meV}$  with open boundary conditions of 50 sites along  $y$ -axis. (d)  $K_0 = 10\text{meV}$ ,  $v_0 = 50\text{meV}$ . The red points in (a), (b), and (d) label the Weyl nodes. The red line in (c) stands for the Fermi arc.

subband has a reduced magnetic Brillouin zone:  $-\pi \leq k_x, k_y \leq \pi$  and  $-\pi/q \leq k_z^0 \leq \pi/q$ .

In ReAlX, the Fermi velocity is  $\sim 1\text{eV}\text{\AA}$ , and the lattice constant is  $\sim 10\text{\AA}$ , and then  $t \sim 100\text{meV}$ . The Curie temperature is about  $30\text{K}$ , and then  $|J_0| \sim 2.5\text{meV}$ . From the first-principles calculations,  $|K_0| \sim |D_0| \sim |J_0|$  are of the same order [5–14]. With these parameters, we plot the band structures of  $H_0$  (2) with the CNHMC in Fig. 2. We find that, for the commensurate nesting  $Q = 2\pi/3$ , the Weyl nodes are folded to the boundaries of the magnetic Brillouin zone for a small  $K_0$  (see Fig. 2a). As  $K_0$  increases, the Weyl nodes move towards each other (see Fig. 2b), which may explain the slightly incommensurate behavior of the helimagnetic configuration observed in experiments [10]. For a strong enough  $K_0$ , the Weyl nodes merge together and finally open a gap. The Fermi arcs that connect the Weyl nodes will also evolve from shortening to disappearing; see Fig. 2c (for more details, see [36]). These phenomena reflect the competition between the monopole topology of the Weyl node in momentum space and the trivial topology of the helimagnet in real space. The  $P$ -breaking term  $v_0$  shifts the energy of every Weyl node and does not alter the location of the Weyl nodes (see Fig. 2d).

*Magnetic phase diagram.* We turn to study the magnetic phase diagrams of the model Hamiltonian (1). For a fixed magnetic configuration, which is either the FM or the CNHMC, we compare the ground state energy per site at zero temperature and the free energy  $f$  per site at finite temperature of Eq. (1). For the CNHMC, one takes  $Q = 2\pi/3$  and the FM is given by  $Q = 0$ . To

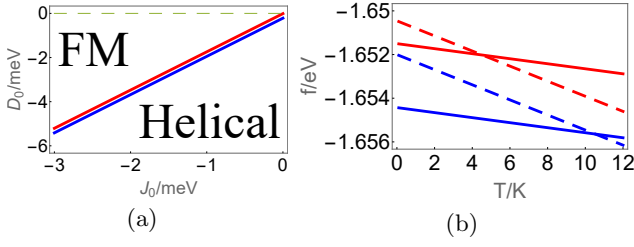


FIG. 3: (color online) The parameters are the same as in Fig. 2a except for  $K_0$ .  $K_0 = 10\text{meV}$  for the red lines and  $K_0 = 50\text{meV}$  for the blue lines. (a) The zero-temperature phase diagram with  $J_0$  versus  $D_0$ . The gray dashed line stands for the case with  $D_0 = 0$ , for which the ground state energy per site is the same for both phases along the lines. Above (below) the lines, the FM (helical) configuration is energetically favored. (b) The free energy per site  $f$  versus temperature  $T$  for  $J_0 = -3\text{meV}$  and  $D_0 = -4\text{meV}$ . The solid (dashed) lines stand for  $f$  with the FM (helical) configuration.

obtain the spectra, we use exact diagonalization in the calculations and choose periodic boundary conditions for a cubic lattice with  $L_x = L_y = L_z = 20$ .

At zero temperature, we find that for a fixed  $J_0$ , the CNHMC is favored for large DM interaction  $D_0$ . The phase boundary moves downward when  $K_0$  increases (see Fig. 3a). At finite temperature, by choosing  $J_0 = -3\text{meV}$ ,  $D_0 = -4\text{meV}$ ,  $K_0 = 10\text{meV}$ , with the other parameters the same as those in Fig. 2a, a phase transition occurs at about  $T_c = 4.5\text{K}$  (Fig. 3b), which is qualitatively consistent with experiments in [9], although the ordered phase is a canted magnetic order instead of the FM. By increasing  $K_0$ ,  $T_c$  also increases (see Fig. 3b).

*CME with CNHMC.* To further explore the effects of the CNHMC in this type of magnetic Weyl semimetals, we study the CME [37]. For an isolated Weyl node given by the low-energy Hamiltonian  $h_w = b_0 + \boldsymbol{\sigma} \cdot (\mathbf{k} - \mathbf{b})$ , where  $\mathbf{b}$  and  $b_0$  denote the shift in momentum and energy, respectively. Its response to the external magnetic field is described by the topological  $\theta$ -term,  $\theta_{\mathbf{r},t} \mathbf{E} \cdot \mathbf{B}$ , with  $\theta_{\mathbf{r},t} = 2(\mathbf{b} \cdot \mathbf{r} - b_0 t)$  [38–41], which originates from the chiral anomaly of the Weyl fermion [42–44] and corresponds to the charge density  $\rho \propto \mathbf{b} \cdot \mathbf{B}$  and current  $\mathbf{j} \propto (\mathbf{b} \times \mathbf{E} - b_0 \mathbf{B})$ . The  $\mathbf{b}$ -related terms contribute to the anomalous Hall effect, while the  $b_0$  term contributes to the CME which is related to the giant negative magnetoresistance [45–48]. In our model Hamiltonian (2),  $b_0 \propto v_0$  and  $\mathbf{b} \propto (0, K_0, 0)$  in the FM limit  $Q = 0$ . For the CNHMC with  $|Q| = 2|k_0|$ ,  $\mathbf{b}$  is not well-defined for small  $K_0$  because the Weyl nodes are close to each other due to band-folding.

To explore the CME with the CNHMC, we apply a uniform magnetic field in the  $z$ -direction in the Hamiltonian (2). In the  $x$ - $y$  plane, the lattice sites are labeled by  $(n, m)$ , and the gauge  $\theta_{(n,m),(n+1,m)}^x = 0$  and  $\theta_{(n,m),(n,m+1)}^y = 2\pi\phi n$  is used [32–34]. Under this gauge, the flux through a unit plaquette is  $2\pi\phi$ . The current

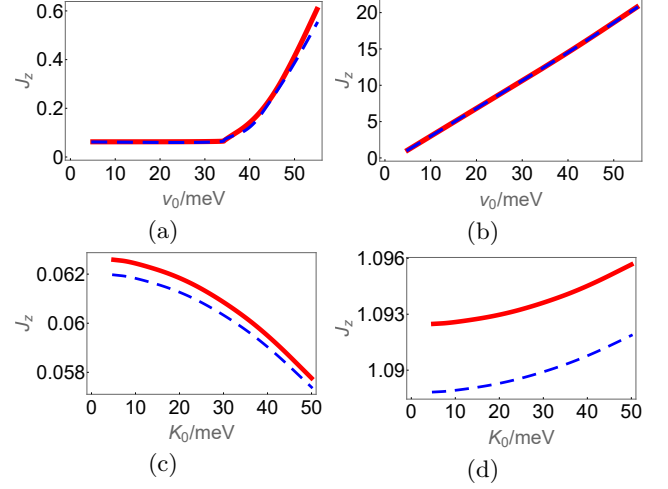


FIG. 4: (color online) The current  $J_z$  of the CME at zero temperature with  $t = t' = 0.1\text{eV}$ ,  $\phi = 1/5$ , and  $L_x = 20$  is shown with periodic boundary conditions for the red solid lines and open boundary conditions for the blue dashed lines.  $\Lambda = \pi/6$ . (a)  $K_0 = 10\text{meV}$ ,  $Q = 2\pi/3$ ; (b)  $K_0 = 10\text{meV}$ ,  $Q = 0$ ; (c)  $v_0 = 5\text{meV}$ ,  $Q = 2\pi/3$ ; (d)  $v_0 = 5\text{meV}$ ,  $Q = 0$ .

arising from the CME reads [45]

$$J_z = \sum_{n,k_y,k_z} \langle \phi_{n,k_y,k_z} | \frac{\partial H_0(k_z)}{\partial k_z} | \phi_{n,k_y,k_z} \rangle n_F(E_n(k_y, k_z)), \quad (6)$$

where  $n_F$  is the Fermi distribution function. The periodic boundary conditions in the  $y$ - and  $z$ -directions are used. Both periodic and open boundary conditions are considered in the  $x$ -direction with a length  $L_x$ . We set  $\phi = 1/5$ .

To see the CME in Weyl semimetals, a cutoff  $\Lambda \ll \pi$  in the summation of  $k_z$  is taken instead of summing over the whole Brillouin zone and the current grows linearly in  $b_0$  for a Weyl semimetal [45]. With this scenario, we calculate the CME with  $L_x = 20$ ,  $\Lambda = \pi/6$ , and plot  $J_z$  by varying  $v_0$  and  $K_0$  at zero temperature in Fig. 4. We find that the Fermi arc states have a negative contribution to  $J_z$  because  $J_z$  under open boundary conditions is slightly smaller than that under periodic conditions. In the FM case,  $J_z$  is linearly dependent on  $v_0$  as expected (see Fig. 4b), while for the CNHMC,  $J_z$  remains a constant when  $v_0 < 3K_0$  and then grows (see Fig. 4a). For a large  $v_0$ , the folded Weyl nodes are separated far enough and isolated (see Fig. 2d). Therefore, the linear behavior of  $J_z$  versus  $v_0$  is expected. In the  $J_z$  constant regime,  $J_z$  decreases when  $K_0$  increases. This shows that the Kondo coupling suppresses the CME with the CNHMC (see Fig. 4c) while it raises the CME with the FM order (see Fig. 4d). The key observation is that the CME in the CNHMC is about 20 times smaller than that in the FM order, which may explain the nearly zero behavior observed near  $T = 12.8\text{K}$  in CeAlGe [9].

*Conclusions.* We constructed a minimal lattice model with Kondo, FM, and DM interactions for the Weyl

semimetal in which both  $\Theta$  and  $P$  symmetries are broken, which caught the key correlated physics in  $\text{ReAlX}$ . We found that the CNHMC induces a magnetic Brillouin zone in the band structure of the conduction electrons. The magnetic phase transitions from the ordered phase to the CNHMC were explored. We also calculated the CME with the CNHMC, which is about 20 times smaller

than that with the FM order. This may provide an explanation for the anomalous transport phenomena and nearly zero magnetoresistance observed in  $\text{CeAlGe}$ .

The authors thank Long Liang and Yong-Shi Wu for useful discussions. This work is supported by the National Natural Science Foundation of China with Grant No. 12174067 (XL, YMZ, and YY).

- 
- [1] S.-Y. Xu, N. Alidoust, G.-Q. Chang, H. Lu, B. Singh, I. Belopolski, D. S. Sanchez, X. Zhang, G. Bian, H. Zheng, M.-A. Hsuanu, Y. Bian, S.-M. Huang, C.-H. Hsu, T.-R. Chang, H.-T. Jeng, A. Bansil, T. Neupert, V. N. Strocov, H. Lin, S. Jia, M. Z. Hasan, “Discovery of Lorentz-violating type II Weyl fermions in  $\text{LaAlGe}$ ”, *Sci. Adv.* **3**, e1603266 (2017).
  - [2] G.-Q. Chang, B. Singh, S.-Y. Xu, G. Bian, S.-M. Huang, C.-H. Hsu, I. Belopolski, N. Alidoust, D. S. Sanchez, H. Zheng, H. Lu, X. Zhang, Y. Bian, T.-R. Chang, H.-T. Jeng, A. Bansil, H. Hsu, S. Jia, T. Neupert, H. Lin, and M. Z. Hasan, “Magnetic and noncentrosymmetric Weyl fermion semimetals in the  $\text{RAlGe}$  family of compounds ( $\text{R} = \text{rare earth}$ )”, *Phys. Rev. B* **97**, 041104(R) (2018).
  - [3] D. S. Sanchez, G. Chang, I. Belopolski, H. Lu, J.-X. Yin, N. Alidoust, X. Xu, T. A. Cochran, X. Zhang, Y. Bian, S. S. Zhang, Y.-Y. Liu, J. Ma, G. Bian, H. Lin, S.-Y. Xu, S. Jia, and M. Z. Hasan, “Observation of Weyl fermions in a magnetic non-centrosymmetric crystal”, *Nat. Commun.* **11**, 3356 (2020).
  - [4] D. Destrz, L. Das, S. S. Tsirkin, Yang Xu, T. Neupert, J. Chang, A. Schilling, A. G. Grushin, J. Kohlbrecher, L. Keller, P. Puphal, E. Pomjakushina and J. S. White, “Magnetism and anomalous transport in the Weyl semimetal  $\text{PrAlGe}$ : possible route to axial gauge fields”, *npj Quantum Mater.* **5**, 5 (2020).
  - [5] H.-Y. Yang, B. Singh, B. Lu, C.-Y. Huang, F. Bahrami, W.-C. Chiu, D. Graf, S.-M. Huang, B. Wang, H. Lin, D. Torchinsky, A. Bansil, and F. Tafti, “Transition from Intrinsic to Extrinsic Anomalous Hall Effect in the ferromagnetic Weyl Semimetal  $\text{PrAlGe}_{1-x}\text{Si}_x$ ”, *APL Mater.* **8**, 011111 (2020).
  - [6] J. Gaudet, H.-Y. Yang, S. Baidya, B. Lu, G. Xu, Y. Zhao, J. A. Rodriguez-Rivera, C. M. Hoffmann, D. E. Graf, D. H. Torchinsky, P. Nikolić, D. Vanderbilt, F. Tafti, and C. L. Broholm, “Weyl-mediated helical magnetism in  $\text{NdAlSi}$ ”, *Nat. Mater.* **20**, 1650 (2021).
  - [7] R. Yamada, T. Nomoto, A. Miyake, T. Terakawa, A. Kikkawa, R. Arita, M. Tokunaga, Y. Taguchi, Y. Tokura, and M. Hirschberger, “Nernst effect of high-mobility Weyl electrons in  $\text{NdAlSi}$  enhanced by a fermi surface nesting instability”, *Phys. Rev. X* **14**, 021012 (2024).
  - [8] H.-Y. Yang, B. Singh, J. Gaudet, B. Lu, C.-Y. Huang, W.-C. Chiu, S.-M. Huang, B. Wang, F. Bahrami, B. Xu, J. Franklin, I. Sochnikov, D. E. Graf, G. Xu, Y. Zhao, C. M. Hoffman, H. Lin, D. H. Torchinsky, C. L. Broholm, A. Bansil, and F. Tafti, “Noncollinear ferromagnetic Weyl Semimetal with Anisotropic Anomalous Hall Effect”, *Phys. Rev. B* **103**, 115143 (2021).
  - [9] N. C. Drucker, T. Nguyen, F. Han, P. Siriviboon, X. Luo, N. Andrejevic, Z. Zhu, G. Bednik, Q. T. Nguyen, Z. Chen, L. K. Nguyen, T. Liu, T. J. Williams, M. B. Stone, A. I. Kolesnikov, S. Chi, J. Fernandez-Baca, C. S. Nelson, A. Alatas, T. Hogan, A. A. Puzetzy, S. Huang, Y. Yu, and M. Li, “Topology stabilized fluctuations in a magnetic nodal semimetal”, *Nat. Commun.* **14**, 5182 (2023).
  - [10] X. Yao, J. Gaudet, R. Verma, D. E. Graf, H.-Y. Yang, F. Bahrami, R. Zhang, A. A. Aczel, S. Subedi, D. H. Torchinsky, J. Sun, A. Bansil, S.-M. Huang, B. Singh, P. Blaha, P. Nikolić, and F. Tafti, “Large Topological Hall Effect and Spiral Magnetic Order in the Weyl Semimetal  $\text{SmAlSi}$ ”, *Phys. Rev. X* **13**, 011035 (2023).
  - [11] H.-Y. Yang, J. Gaudet, R. Verma, S. Baidya, F. Bahrami, X. Yao, C.-Y. Huang, L. DeBeer-Schmitt, A. A. Aczel, G. Xu, H. Lin, A. Bansil, B. Singh, and F. Tafti, “Stripe helical magnetism and two regimes of anomalous Hall effect in  $\text{NdAlGe}$ ”, *Phys. Rev. Materials* **7**, 034202 (2023).
  - [12] A. Laha, A. K. Kundu, N. Aryal, E. S. Bozin, J. Yao, S. Paone, A. Rajapitamahuni, E. Vescovo, T. Valla, M. Abeykoon, R. Jing, W. Yin, A. N. Pasupathy, M. Liu, and Q. Li, “Electronic structure, magnetic and transport properties of antiferromagnetic Weyl semimetal  $\text{GdAlSi}$ ”, *Phys. Rev. B* **109**, 035120 (2024).
  - [13] N. Kikugawa, S. Uji, and T. Terashima, “Anomalous Hall effect in the magnetic Weyl semimetal  $\text{NdAlGe}$  with plateaus observed at low temperatures”, *Phys. Rev. B* **109**, 035143 (2024).
  - [14] J. Nag, B. Das, S. Bhowal, Y. Nishioka, B. Bandyopadhyay, S. Kumar, K. Kuroda, A. Kimura, K. G. Suresh, and A. Alam, “ $\text{GdAlSi}$ : An antiFM topological Weyl semimetal with non-relativistic spin splitting”, *Phys. Rev. B* **110**, 224436 (2024).
  - [15] H.-R. Chang, J. Zhou, S.-X. Wang, W.-Y. Shan, and D. Xiao, “RKKY interaction of magnetic impurities in Dirac and Weyl semimetals”, *Phys. Rev. B* **92**, 241103(R) (2015).
  - [16] J.-H. Sun, D.-H. Xu, F.-C. Zhang, and Y. Zhou, “Magnetic impurity in a Weyl semimetal”, *Phys. Rev. B* **92**, 195124 (2015).
  - [17] S.-X. Wang, H.-R. Chang, and J. Zhou, “RKKY interaction in three-dimensional electron gases with linear spin-orbit coupling”, *Phys. Rev. B* **96**, 115204 (2017).
  - [18] B. Göbel, I. Mertig, O. A. Tretiakov, “Beyond skyrmions: Review and perspectives of alternative magnetic quasiparticles”, *Physics Reports* **895**, 1 (2021).
  - [19] A. K. Mitchell and L. Fritz, “Kondo effect in three-dimensional Dirac and Weyl systems”, *Phys. Rev. B* **92**, 121109(R) (2015).
  - [20] B. A. Bernevig, C. Felser, and H. Beidenkopf, “Progress and prospects in magnetic topological materials”, *Nature* **603**, 41 (2022).
  - [21] Z. Wang, Y. Su, S.-Z. Lin, and C. D. Batista, “Meron, Skyrmion, and Vortex Crystals in Centrosymmetric



- Tetragonal Magnets”, *Phys. Rev. B* **103**, 104408 (2021).
- [22] J. Repicky, P.-K.Wu, T. Liu, J. P. Corbett, T. Zhu, S. Cheng, A. S. Ahmed, N. Takeuchi, J. Guerrero-Sanchez, M. Randeria, R. K. Kawakami, and J. A. Gupta, “Atomic-Scale Visualization of Topological Spin Textures in the Chiral Magnet MnGe”, *Science* **374**, 1484 (2021).
- [23] S. Luo and L. You, “Skyrmion Devices for Memory and Logic Applications”, *APL Mater.* **9**, 050901 (2021).
- [24] V. Rogers, S. Chaudhary, R. Nguyen, and J. A. Incorvia, “Flat bands and multi-state memory devices from chiral domain wall superlattices in magnetic Weyl semimetals”, arXiv:2303.16918.
- [25] F.-Y. Li, X. Luo, X. Dai, Y. Yu, F. Zhang, and G. Chen, “Hybrid Weyl semimetal”, *Phys. Rev. B* **94**, 121105(R) (2016).
- [26] T. M. McCormick, I. Kimchi, and N. Trivedi, “Minimal models for topological Weyl semimetals”, *Phys. Rev. B* **95**, 075133 (2017).
- [27] Y. Yu, “Seiberg-Witten monopoles: Weyl metal coupled to chiral magnets”, arXiv: 1605.00093.
- [28] See supplemental materials, Sec. I.
- [29] H.-R. Chang, J. H. Zhou, S.-X. Wang, W.-Y. Shan, and D. Xiao, “RKKY interaction of magnetic impurities in Dirac and Weyl semimetals”, *Phys. Rev. B* **92**, 241103 (2015).
- [30] M. V. Hosseini and M. Askari, “Ruderman-Kittel-Kasuya-Yosida interaction in Weyl semimetals”, *Phys. Rev. B* **92**, 224435 (2015).
- [31] N. Nagaosa, X. Z. Yu, Y. Tokura, “Gauge fields in real and momentum spaces in magnets: monopoles and skyrmions”, *Phil. Trans. R. Soc. A* **370**, 5806 (2012).
- [32] M. Kohmoto, “Zero modes and the quantized Hall conductance of the two-dimensional lattice in a magnetic field”, *Phys. Rev. B* **39**, 11943 (1989).
- [33] Y. Hatsugai and M. Kohmoto, “Energy spectrum and the quantum Hall effect on the square lattice with next-nearest-neighbor hopping”, *Phys. Rev. B* **42**, 8282 (1990).
- [34] Y. Hatsugai, “Edge states in the integer quantum Hall effect and the Riemann surface of the Bloch function”, *Phys. Rev. B* **48**, 11851 (1993).
- [35] See supplemental materials, Sec. II.
- [36] See supplemental materials, Sec. III.
- [37] K. Fukushima, D. E. Kharzeev, and H. J. Warringa, “Chiral magnetic effect”, *Phys. Rev. D* **78**, 074033 (2008).
- [38] A. A. Zyuzin and A. A. Burkov, “Topological response in Weyl semimetals and the chiral anomaly”, *Phys. Rev. B* **86**, 115133 (2012).
- [39] D. T. Son and N. Yamamoto, “Berry Curvature, Triangle Anomalies, and the Chiral Magnetic Effect in Fermi Liquids”, *Phys. Rev. Lett.* **109**, 181602 (2012).
- [40] P. Goswami and S. Tewari, “Axionic field theory of (3+1)-dimensional Weyl semimetals”, *Phys. Rev. B* **88**, 245107 (2013).
- [41] A. G. Grushin, “Consequences of a condensed matter realization of Lorentz-violating QED in Weyl semi-metals”, *Phys. Rev. D* **86**, 045001 (2012).
- [42] S. L. Adler, “Axial-Vector Vertex in Spinor Electrodynamics”, *Phys. Rev.* **177**, 2426 (1969).
- [43] J. S. Bell and R. Jackiw, “A PCAC puzzle:  $\pi_0 \rightarrow \gamma\gamma$  in the  $\sigma$ -model”, *Il Nuovo Cimento A* **60**, 47 (1969).
- [44] H. B. Nielsen, and M. Ninomiya, “The Adler-Bell-Jackiw anomaly and Weyl fermions in a crystal”, *Physics Letters B* **130**, 389 (1983).
- [45] M. M. Vazifeh and M. Franz, “Electromagnetic Response of Weyl Semimetals”, *Phys. Rev. Lett.* **111**, 027201 (2013).
- [46] A. Burkov, “Chiral anomaly and transport in Weyl metals”, *Journal of Physics: Condensed Matter* **27**, 113201 (2015).
- [47] D. T. Son and B. Z. Spivak, “Chiral anomaly and classical negative magnetoresistance of Weyl metals”, *Phys. Rev. B* **88**, 104412 (2013).
- [48] X. Huang, L. Zhao, Y. Long, P. Wang, D. Chen, Z. Yang, H. Liang, M. Xue, H. Weng, Z. Fang, X. Dai, and G. Chen, “Observation of the Chiral-Anomaly-Induced Negative Magnetoresistance in 3D Weyl Semimetal TaAs”, *Phys. Rev. X* **5**, 031023 (2015).